

PointAlign: Feature-Level Alignment Regularization for 3D Vision-Language Models

Yuanhao Su^{1,2}, Shaofeng Zhang^{1*}, Xiaosong Jia³, Qi Fan⁴
¹University of Science and Technology of China, ²Fuzhou University,
³Fudan University, ⁴Nanjing University
yharoldsu0627@gmail.com, sfzhang@ustc.edu.cn

Abstract

*The development of 3D Vision-Language Models (VLMs), crucial for applications in robotics, autonomous driving, and augmented reality, is severely constrained by the scarcity of paired 3D-text data. Existing methods rely solely on next-token prediction loss, using only language tokens for supervision. This results in inefficient utilization of limited 3D data and leads to a significant degradation and loss of valuable geometric information in intermediate representations. To address these limitations, we propose PointAlign, a novel feature-level alignment regularization method. PointAlign explicitly supervises intermediate point cloud tokens to preserve fine-grained 3D geometric-semantic information throughout the language modeling process. Specifically, we constrain the intermediate point cloud tokens within the LLM to align with visual input tokens via a consistency loss. By training only a lightweight alignment projector and LoRA adapters, PointAlign achieves explicit feature-level supervision with minimal computational overhead, effectively preventing geometric degradation. Extensive experiments on ModelNet40 and Objaverse datasets demonstrate that our method achieves **2.08 pp** improvement on average for classification tasks, with a substantial **7.50 pp** gain on the challenging open-vocabulary Objaverse classification task and **4.88 pp** improvement on 3D object captioning evaluated by Qwen2-72B-Instruct, validating the effectiveness of PointAlign. Code is publicly available at <https://github.com/yharoldsu0627/PointAlign>.*

1. Introduction

While 2D vision-language models (VLMs) [3, 22] have achieved remarkable success through large-scale image-text datasets that enable effective cross-modal alignment [32, 37], 3D vision-language models remain comparatively underdeveloped despite their importance for applications in

robotics [48, 55], autonomous driving [23, 26], and augmented reality [1, 8]. A fundamental challenge in 3D VLM development is the scarcity of high-quality 3D-text paired data—unlike easily accessible 2D images [30], 3D point clouds [41] require expensive acquisition, resulting in smaller datasets with often simplistic textual descriptions [34]. This data limitation poses a core research question: **how to maximize knowledge extraction from scarce supervision for 3D understanding**.

Recent efforts such as PointLLM [42], ShapeLLM [28], and MiniGPT-3D [33] have made progress in addressing these issues. PointLLM and ShapeLLM achieve competitive performance via full-model fine-tuning at substantial computational cost, while MiniGPT-3D reduces costs by leveraging 2D VLM priors. However, these methods optimize through language modeling objectives, which only reward geometric features that directly facilitate next-token prediction. This creates a critical issue: structural cues valuable for spatial reasoning but orthogonal to immediate language tasks may be discarded during training, a degradation we confirm in our feature quality analysis (see Figure 3). Recent work on 2D vision-language models [19, 21, 45] has shown that without explicit visual supervision, representational quality degrades across network depth. In the context of point cloud understanding, this problem is amplified by limited 3D training data. Point cloud networks process information hierarchically: initial layers establish object-level context, intermediate layers resolve part-level geometry, and final layers produce language outputs [45]. Therefore, preserving structural information throughout the forward pass is critical for accurate 3D reasoning.

To address this, we propose PointAlign, a novel feature-level alignment regularization method. Our method is built on a key insight: the representations from the initial stage already capture fine-grained geometric and semantic details, serving as an ideal internal supervision target. We directly align the LLM’s intermediate point cloud tokens with these high-quality, initial-stage features. This alignment is enforced by a consistency loss during the second

*Shaofeng Zhang is the corresponding author

training stage. This approach introduces explicit geometric guidance with minimal overhead, as we only update a lightweight alignment projector (only 8.39M parameters) and LoRA adapters while freezing all pre-trained modules.

We conduct extensive experiments on several 3D vision-language benchmarks, including 3D classification and captioning. Results show that our alignment regularization improves performance across nearly all evaluated tasks, confirming that explicit feature-level supervision helps better preserve geometric structure (as validated by Figure 3) and exploit limited 3D data (as demonstrated in Figure 4). On average, PointAlign improves classification accuracy by **2.08 pp** on ModelNet40 and Objaverse. Notably, it achieves a striking **7.50 pp** gain on the challenging open-vocabulary Objaverse classification task. For 3D object captioning on Objaverse, evaluated by Qwen2-72B-Instruct, our method outperforms the baseline by a significant **4.88 pp**, demonstrating strong generalization in open-domain 3D vision-language scenarios of the proposed PointAlign.

2. Related Work

Large 3D Point Cloud-Language Models. The success of large language models in reasoning and generalization has motivated efforts to develop 3D point cloud-language understanding systems. Initial methods [6, 9, 13, 25, 27, 40, 43, 44, 49, 56] adopt an indirect approach by converting 3D shapes into multiple 2D projections, then leveraging pre-trained vision-language models for cross-modal alignment [50–52]. While computationally efficient, this rendering-based pipeline discards native geometric structure, hindering models from capturing spatial relationships inherent to 3D data. To address this limitation, recent work [10, 28, 29, 33, 42] directly processes point cloud tokens through learned projection modules that bridge the gap between 3D encoders and language models. Full model fine-tuning approaches like PointLLM [42] and ShapeLLM [28] achieve strong performance but at significant computational cost. For example, PointLLM-13B demands over 200 GPU-hours on high-end accelerators. MiniGPT-3D [33] mitigates this burden by incorporating 2D vision-language priors to facilitate 3D-text alignment, achieving comparable results with substantially reduced training resources. Beyond training efficiency, recent work has also explored inference acceleration for 3D MLLMs through visual token pruning techniques [14].

Representation Supervision in Multimodal LLMs.

Recent studies on 2D vision-language models reveal that visual embeddings can lose fidelity across network depth when supervision signals are weak [18–20]. To address this issue, reconstruction-based approaches [11, 38, 39, 53, 54] have been proposed to supervise intermediate representations by recovering visual inputs, demonstrating effectiveness in retaining fine-grained details for 2D understanding

tasks. However, 3D point cloud reasoning demands fundamentally different capabilities—models must capture structural relationships and geometric configurations that extend beyond low-level visual features [36, 47]. In the 3D point cloud domain, methods leveraging pre-trained 3D encoders [15, 21] provide specialized geometric supervision by distilling knowledge from foundation models trained on large-scale 3D point cloud data, though this introduces additional computational overhead during the training phase.

3. The Proposed PointAlign

Preliminaries: MiniGPT-3D

MiniGPT-3D [33] is an efficient 3D large language model that aligns 3D point clouds with LLMs by leveraging priors from 2D vision-language models. Given a point cloud $\mathbf{P} \in \mathbb{R}^{n \times d}$, where n denotes the number of points and d represents the feature dimension of each point, the point cloud encoder $f_{pc}(\cdot)$ first encodes it into 3D features $f_{pc}(\mathbf{P}) \in \mathbb{R}^{m \times D}$, where m is the length of the feature sequence and D is the feature dimension. Subsequently, an MLP projection layer $f_{MLP}(\cdot)$ projects the point cloud features into the semantic space of Q-Former. Next, Q-Former [22] $f_{QF}(\cdot)$ queries the point cloud features through learnable query vectors $\mathbf{Q} \in \mathbb{R}^{o \times D_1}$, yielding point cloud tokens $\bar{\mathbf{Q}} = f_{QF}(f_{MLP}(f_{pc}(\mathbf{P})), \mathbf{Q}) \in \mathbb{R}^{o \times D_1}$, where o is the number of queries and D_1 is the hidden dimension of Q-Former. Finally, the modality projector maps the Q-Former output to the input space of the LLM as $\mathbf{T}_{pc} \in \mathbb{R}^{o \times C}$, where C is the shared dimension between point cloud and text tokens. The point cloud features are concatenated with text features $\mathbf{T} = [\mathbf{T}_{text}, \mathbf{T}_{pc}]$ and fed into the large language model $f_{llm}(\cdot)$ to autoregressively generate text responses. The first three recipes of MiniGPT-3D train the Q-Former, projector, and LLM using point cloud-text paired data, with the training objective being the cross-entropy loss for next token prediction $\mathcal{L}_{ntp} = \text{CrossEntropy}(h(G), \bar{\mathbf{T}})$, where $h(\cdot)$ is the LLM’s tokenizer, G is the ground truth answer text, and $\bar{\mathbf{T}}$ is the predicted probability distribution.

3.1. Overall Architecture

As illustrated in Figure 1, our method employs a two-stage training strategy to enhance the geometric understanding capabilities of MiniGPT-3D. Stage 1 is the MiniGPT-3D pre-training, which adopts the three training recipes of MiniGPT-3D and trains the point cloud encoder, MLP projection layer, Q-Former, modality projector, and LLM backbone. Stage 2 is the alignment regularization fine-tuning, which freezes the point cloud encoder, MLP projection layer, Q-Former, and modality projector, and only trains the LoRA layers [12] of the LLM and the newly introduced alignment projector composed of 3 linear layers. Note that the alignment projector is used only during training and is discarded at inference, introducing zero addi-

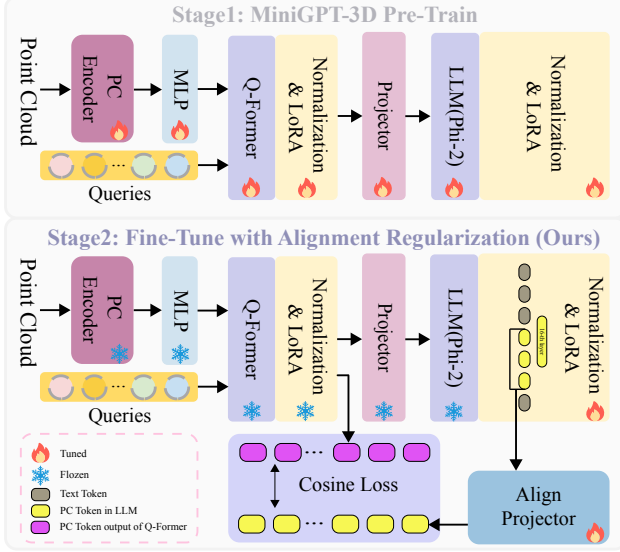


Figure 1. Overview of our method. Stage 1 adopts the three training recipes of MiniGPT-3D for pre-training. Stage 2 freezes the point cloud encoder, MLP, Q-Former, and modality projector, and only trains the LoRA layers of the LLM and the alignment projector. The alignment projector aligns the latent representations of point cloud tokens in the LLM with the Q-Former output through cosine similarity loss. Flame icons indicate trainable modules, and snowflakes indicate frozen modules.

tional inference overhead.

The core idea is to align the point cloud tokens in the intermediate layers of trainable LLM with the point cloud tokens output by frozen Q-Former. Specifically, the alignment projector maps the point cloud tokens $\mathbf{T}_{pc}^{(\ell)}$ at the ℓ -th layer of the LLM to the Q-Former feature space, constraining the representations to remain consistent with the Q-Former output $\bar{\mathbf{Q}}$ through cosine similarity loss, thereby preserving richer point cloud geometric and semantic information during the language modeling process.

3.2. Point Cloud Representation Alignment

The training of MiniGPT-3D and other 3D understanding methods [42] is commonly optimized solely through \mathcal{L}_{ntp} , leading to point cloud features only receiving indirect supervision from text prediction. Let $\mathbf{T}_{pc}^{(\ell)} \in \mathbb{R}^{o \times c}$ denote the point cloud tokens at the ℓ -th layer of the LLM (The specific choice of ℓ is detailed in the experimental settings). During training, no explicit regularization is applied to the $\mathbf{T}_{pc}^{(\ell)}$, potentially losing fine-grained 3D geometric information. To address this, we propose to align the point cloud tokens in the LLM’s intermediate layers with the Q-Former output.

We select the Q-Former output $\bar{\mathbf{Q}} \in \mathbb{R}^{o \times D_1}$ (features after Q-Former and its subsequent Normalization and LoRA layers) as the alignment target rather than the point cloud

Algorithm 1 Fine-tune with Alignment Regularization.

Require: Point cloud \mathbf{P} , text prompt features \mathbf{T}_{text} , ground truth G , pre-trained components from Stage 1, hyperparameters λ and ℓ

Ensure: Fine-tuned LLM with LoRA and alignment projector f_π

- 1: Freeze: $f_{pc}, f_{MLP}, f_{QF}, f_{proj}$
 - 2: Initialize LoRA in f_{llm} and 3-layer projector f_π {Eq. (1)}
 - 3: **for** each training batch **do**
 - 4: $\bar{\mathbf{Q}} \leftarrow f_{QF}(f_{MLP}(f_{pc}(\mathbf{P})), \mathbf{Q})$ {Q-Former output}
 - 5: $\mathbf{T}_{pc} \leftarrow f_{proj}(\bar{\mathbf{Q}})$ {Modality projection}
 - 6: $\mathbf{T} \leftarrow [\text{BOS}, \mathbf{T}_{text}, \mathbf{T}_{pc}, h(G)]$
 - 7: $s \leftarrow 1 + |\mathbf{T}_{text}|, e \leftarrow s + 32$ {PC token positions}
 - 8: $\bar{\mathbf{T}}, \{H^{(1)}, \dots, H^{(L)}\} \leftarrow f_{llm}(\mathbf{T})$ {Output & hidden states}
 - 9: $\mathbf{T}_{pc}^{(\ell)} \leftarrow H^{(\ell)}[:, s : e, :]$ {Extract PC tokens from Layer ℓ }
 - 10: $\bar{\mathbf{Q}} \leftarrow f_\pi(\mathbf{T}_{pc}^{(\ell)})$ {Project to Q-Former space}
 - 11: $\mathcal{L}_{ntp} \leftarrow \text{CrossEntropy}(h(G), \bar{\mathbf{T}})$
 - 12: \mathcal{L}_{align} by Eq. (2) with $\bar{\mathbf{Q}}^{\text{detach}}$
 - 13: \mathcal{L}_{total} by Eq. (3)
 - 14: Update θ_{LoRA} and θ_π via $\nabla \mathcal{L}_{total}$
 - 15: **end for**
-

encoder output or deep LLM representations. The rationale behind this choice is that the Q-Former has learned the mapping between geometry and semantics through point cloud-text pairs during Stage 1 training [22, 33], and its output contains both geometric and semantic information. Compared to the point cloud encoder that only captures geometric features, the Q-Former output is more suitable for supervising the LLM’s intermediate layers. Meanwhile, $\bar{\mathbf{Q}}$ is primarily supervised by point cloud-text pairs directly before entering the LLM, preserving more original geometric details, while deep LLM representations may have lost 3D information through multiple layers of language modeling.

We further propose an alignment projector $f_\pi : \mathbb{R}^c \rightarrow \mathbb{R}^{D_1}$, which maps the point cloud tokens at the ℓ -th layer of the LLM to the feature space of Q-Former. As shown in Figure 1, the projector consists of three linear layers and two SiLU [7] activation functions, providing sufficient non-linear transformation capacity while maintaining computational efficiency. Let \mathbf{W}_i and \mathbf{b}_i denote the weight matrix and bias vector of the i -th linear transformation. The mapping process is formulated as:

$$\begin{aligned}
 \mathbf{h}^{(1)} &= \mathbf{W}_1 \cdot \mathbf{T}_{pc}^{(\ell)} + \mathbf{b}_1, \\
 \mathbf{h}^{(2)} &= \mathbf{W}_2 \cdot \text{SiLU}(\mathbf{h}^{(1)}) + \mathbf{b}_2, \\
 \tilde{\mathbf{Q}} &= \mathbf{W}_3 \cdot \text{SiLU}(\mathbf{h}^{(2)}) + \mathbf{b}_3,
 \end{aligned} \tag{1}$$

Table 1. Performance evaluation of generative 3D object classification on ModelNet40 test set and Objaverse dataset. Classification accuracy (%) is evaluated using two prompt formats: Instruction-based (I) “What is this?” and Completion-based (C) “This is an object of”, with average scores provided. Best and second-best performances are highlighted in bold and underlined, respectively.

Model	Reference	LLM Size	3D Data Size	Input	ModelNet40			Objaverse			Average
					(I)	(C)	Average	(I)	(C)	Average	
InstructBLIP-7B [3]	NeurIPS,23	7B	0K	Single-V. Img.	17.67	22.81	20.24	21.50	26.00	23.75	22.00
InstructBLIP-13B [3]	NeurIPS,23	13B	0K	Single-V. Img.	21.56	21.92	21.74	21.50	21.50	21.50	21.62
LLaVA-7B [24]	CVPR,24	7B	0K	Single-V. Img.	27.11	21.68	24.40	37.50	30.00	33.75	29.07
LLaVA-13B [24]	CVPR,24	13B	0K	Single-V. Img.	27.71	27.76	27.74	39.50	35.50	37.50	32.62
GPT-4o mini [16]	OpenAI	-	0K	Single-V. Img.	22.00	23.10	22.55	39.00	35.00	37.00	29.78
Point-Bind LLM [10]	arXiv,23	7B	-	Point Cloud	46.60	45.02	45.81	7.50	7.58	7.54	26.68
GPT4Point [29]	CVPR,24	2.7B	660K	Point Cloud	21.39	21.07	21.23	49.00	46.50	47.75	34.49
PointLLM-7B [42]	ECCV,24	7B	730K	Point Cloud	51.34	50.36	50.85	62.00	63.00	62.50	56.68
PointLLM-13B [42]	ECCV,24	13B	730K	Point Cloud	51.70	52.67	52.19	61.50	63.00	62.25	57.22
MiniGPT-3D [33]	MM,24	2.7B	730K	Point Cloud	61.99	60.49	61.24	<u>65.00</u>	<u>68.50</u>	<u>66.75</u>	<u>64.00</u>
Ours	-	2.7B	730K	Point Cloud	<u>61.55</u>	60.78	<u>61.17</u>	72.50	69.50	71.00	66.08

where $\mathbf{W}_1 \in \mathbb{R}^{d_h \times C}$, $\mathbf{W}_2 \in \mathbb{R}^{d_h \times d_h}$, $\mathbf{W}_3 \in \mathbb{R}^{D_1 \times d_h}$, and d_h is the hidden dimension. The SiLU activation function is defined as $\text{SiLU}(x) = x \cdot \sigma(x)$, where $\sigma(x)$ is the sigmoid function. The final output is $\mathbf{Q} \in \mathbb{R}^{o \times D_1}$.

The alignment loss is defined using cosine similarity [31], as shown in Figure 1. We adopt the cosine loss as an alignment loss because it focuses on feature direction rather than magnitude, making it well-suited for aligning representations across different feature spaces. Given the mapped features $\tilde{\mathbf{Q}}$ and the Q-Former output $\bar{\mathbf{Q}}$, the alignment loss is:

$$\mathcal{L}_{align} = -\frac{1}{o} \sum_{i=1}^o \frac{\tilde{\mathbf{Q}}_i^\top \bar{\mathbf{Q}}_i}{\|\tilde{\mathbf{Q}}_i\|_2 \|\bar{\mathbf{Q}}_i\|_2}, \quad (2)$$

where i denotes the i -th query token.

3.3. Training Objective

The total loss function consists of the next token prediction loss and the alignment loss:

$$\mathcal{L}_{total} = \mathcal{L}_{ntp} + \lambda \mathcal{L}_{align}, \quad (3)$$

where λ is a hyperparameter balancing the two losses. During Stage 2, we freeze the parameters of the point cloud encoder, MLP projection layer, Q-Former, and modality projector, and only train the LoRA layers of the LLM and the alignment projector f_π . The Q-Former output $\bar{\mathbf{Q}}$ is treated as a constant when computing the alignment loss and does not participate in gradient backpropagation, preserving the point cloud-language alignment knowledge learned in Stage 1. This training strategy preserves pre-trained knowledge while efficiently fine-tuning the LLM through LoRA and preserving point cloud geometric and semantic information through alignment constraints.

3.4. Algorithm Pseudo Code

Algorithm 1 outlines the complete training procedure of our alignment regularization approach. As shown in the pseudo-code, the implementation is straightforward yet effective: by freezing pre-trained modules and introducing a lightweight alignment projector (3 linear layers), followed by an alignment loss, we achieve significant improvements in geometric understanding with minimal computational overhead and easy integration into existing pipelines.

4. Experiments

4.1. Experimental Settings

We employ Phi-2 [17] as the foundational component for the large language model and utilize PointBERT [46] to extract semantic features from 3D point clouds. All experiments are conducted on NVIDIA RTX 4090 GPUs equipped with 24GB of memory. We adopt a two-stage training strategy. In the pre-training stage, we follow the first three training stages of MiniGPT-3D [33], using the same data scale, training epochs, and learning rate schedule. In the fine-tuning stage, we train for 10000 iterations on 70k detailed descriptions and dialogue data, with the learning rate linearly decaying from 3e-6 to 1e-6. Meanwhile, we introduce an alignment module consisting of three linear layers with SiLU [7] activation functions to achieve feature dimensionality reduction and alignment. The alignment is applied at the 16-th layer of the Phi-2 model. The training data is sourced from the point-text instruction dataset [42], encompassing both brief description instructions and complex instruction samples. Following the data split criteria established by PointLLM [42], we reserve 200 object sam-

Table 2. Performance evaluation of 3D object captioning on the Objaverse dataset. Evaluation metrics include Qwen2 evaluation and traditional metrics. Bold and underlined values represent the best and second-best performances, respectively.

Model	Reference	LLM Size	3D Data Size	Input	Qwen2-72B-Instruct	Sentence-BERT	SimCSE	Average
InstructBLIP-7B [3]	NIPS,23	7B	0K	Single-V. Img.	16.10	35.79	36.67	29.52
InstructBLIP-13B [3]	NIPS,23	13B	0K	Single-V. Img.	13.79	33.52	35.60	27.64
LLaVA-1.5-7B [24]	CVPR,24	7B	0K	Single-V. Img.	17.80	39.32	41.08	32.73
LLaVA-1.5-13B [24]	CVPR,24	13B	0K	Single-V. Img.	16.00	39.64	40.90	32.18
GPT-4o mini [16]	OpenAI	-	0K	Single-V. Img.	26.00	38.70	39.13	34.61
Point-Bind LLM [10]	arXiv,23	7B	-	Point Cloud	1.93	27.29	25.35	18.19
GPT4Point [29]	CVPR,24	2.7B	660K	Point Cloud	21.75	41.10	41.24	34.70
PointLLM-7B [42]	ECCV,24	7B	730K	Point Cloud	42.20	48.50	48.92	46.54
PointLLM-13B [42]	ECCV,24	13B	730K	Point Cloud	40.40	49.07	48.41	45.96
MiniGPT-3D [33]	MM,24	2.7B	730K	Point Cloud	<u>48.17</u>	<u>49.54</u>	51.39	<u>49.70</u>
Ours	-	2.7B	730K	Point Cloud	53.05	49.94	<u>51.32</u>	51.44

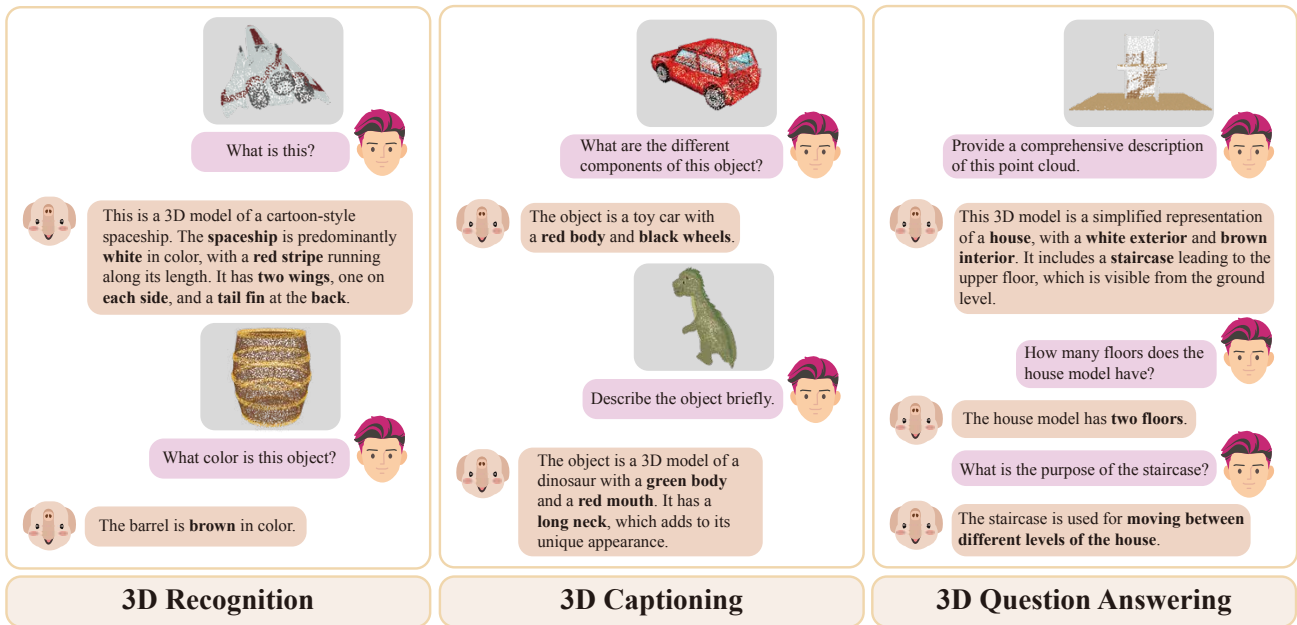


Figure 2. Examples of 3D Object Understanding with Our Model. The figure demonstrates our model’s capabilities in the context of 3D object understanding, showcasing its performance on tasks such as 3D object recognition, description generation, and 3D VQA.

ples for testing and evaluation. Regarding the point cloud input format, each sample comprises $n = 8192$ sampled points, with each point containing $d = 6$ dimensional features that encode both 3D spatial coordinates and corresponding attributes. To validate the effectiveness of our proposed method, we select several state-of-the-art models as baseline comparisons, specifically including 5 open-source 3D models [10, 29, 33, 42] and 5 open-source 2D models [3, 16, 24]. Following GreenGLM [34], we uniformly employ the Qwen2-72B-Instruct [35] model to assess and

score the generation quality of all comparative methods.

4.2. Generative 3D Object Classification

We conduct generative 3D object classification tasks on ModelNet40 [41] and the more challenging open-vocabulary Objaverse [4] dataset. As shown in Table 1, following [28, 42], we adopt two prompt formats for evaluation: instruction-based (I) “What is this?” and completion-based (C) “This is an object of”. For zero-shot classification on the closed-set ModelNet40 dataset, we leverage

Table 3. Qualitative comparison of model outputs for classification and captioning on the Objaverse datasets.

Sample	
Prompt	Briefly caption this 3D model.
Ground Truth	A cartoon black monster like a dragon
InstructBLIP-13B	a black lizard with a sharp tooth in a dark room
LLaVA-13B	A 3D model of a dark, menacing dragon.
3D-LLM	A black and white tiger with long legs, standing on its hind leg.
Point-Bind LLM	The 3D model features a large, ornate gargoyle with a horned helmet, sitting on top of a building.
PointLLM-13B	The 3D model depicts a menacing black dragon, with its mouth opened wide revealing a row of sharp teeth.
MiniGPT-3D	This is a 3D model of a fearsome, black-colored dinosaur. The dinosaur possesses an aggressive stance, with sharp claws extending from its arms and legs. It has long black fangs that seem ready to attack.
PointAlign	the 3d model is a cartoon-style representation of a dragon , characterized by its large, sharp teeth and claws. the dragon is predominantly black in color, with a distinctively long tail. the dragon's mouth is open, suggesting it's in a state of attack or defense. the model is designed to be used in animations, video games, or as a decorative item.

Table 4. Ablation study on loss functions. We evaluate the impact of different loss functions at 16-th layer on classification accuracy.

Loss	ModelNet40		Objaverse		Average
	(I)	(C)	(I)	(C)	
11	61.30	60.58	71.50	69.50	65.72
12	61.51	61.75	69.50	69.50	65.57
cosine	61.55	60.78	72.50	69.50	66.08

Table 5. Ablation study on target layers. We evaluate the impact of different layer indices on classification accuracy (%).

Layer Index	ModelNet40		Objaverse		Average
	(I)	(C)	(I)	(C)	
8	61.47	60.86	69.50	69.50	65.33
12	61.71	60.33	70.50	68.00	65.14
16	61.55	60.78	72.50	69.50	66.08
20	61.30	60.09	70.50	69.00	65.22
24	61.71	60.86	71.00	66.00	64.89
28	61.30	60.94	70.00	67.00	64.81
32	61.67	60.58	70.00	68.00	65.06
12, 16, 20	61.63	60.21	69.00	66.50	64.34

the Qwen2-72B-Instruct model to parse the textual outputs from our method, enabling precise prediction from 40 candidate categories. For the open-vocabulary category recognition task on the Objaverse dataset, we employ Qwen2-72B-Instruct model as semantic judges to verify whether our model’s generated descriptive text refers to the same object category as the ground truth label.

Experimental results demonstrate that our model

Table 6. Ablation study on the weight of the alignment loss λ . We evaluate the impact of different λ at 16-th layer.

λ	ModelNet40		Objaverse		Average
	(I)	(C)	(I)	(C)	
0	60.58	60.29	69.50	68.50	64.72
0.1	61.55	60.78	72.50	69.50	66.08
0.3	61.75	60.21	69.50	67.50	64.74
0.5	61.39	60.94	69.50	68.50	65.08
0.7	61.10	60.94	67.00	68.50	64.39
0.9	61.51	60.66	68.50	68.00	64.67

achieves an average classification accuracy of 66.08%, significantly outperforming all baseline methods. Compared to the current state-of-the-art 3D point cloud model MiniGPT-3D, we achieve a 2.08 pp improvement. More notably, on the Objaverse dataset under the instruction-based prompt, we obtain a substantial improvement of 7.50 pp over MiniGPT-3D. Additionally, the average accuracy reaches 71.00%, representing a 4.25 pp improvement over MiniGPT-3D and a remarkable 8.75 pp gain over PointLLM-13B. This advantage is particularly critical in open-vocabulary scenarios, indicating that our model exhibits stronger generalization capabilities when handling open-domain categories. These results validate the effectiveness of aligning point cloud tokens in the intermediate layers of the LLM with the Q-Former output.

4.3. 3D Object Captioning

The 3D object captioning task requires models to generate accurate and detailed natural language descriptions for input point clouds. We evaluate on the Objaverse dataset using the unified prompt “Caption this 3D model in detail” and employ Qwen2-72B-Instruct, Sentence-BERT, and SimCSE to assess the semantic similarity between model outputs and manual annotations. As shown in Table 2, our model achieves an average score of 51.44, surpassing all baseline methods. In the Qwen2 evaluation, we attain the highest score of 53.05, representing a 4.88 pp improvement over the second-best model MiniGPT-3D and a 10.85 pp gain over PointLLM-7B, while significantly outperforming 2D models such as GPT-4o mini. On the Sentence-BERT and SimCSE metrics, we achieve scores of 49.94 and 51.32, respectively, maintaining comparable performance to MiniGPT-3D. The experimental results demonstrate that our proposed partial token alignment mechanism effectively integrates 3D visual features with language semantic representations, enhancing the perception of fine-grained 3D object details while maintaining semantic accuracy.

4.4. Qualitative Results

Figure 2 shows our model’s performance on 3D recognition, captioning, and 3D question answering tasks. The examples

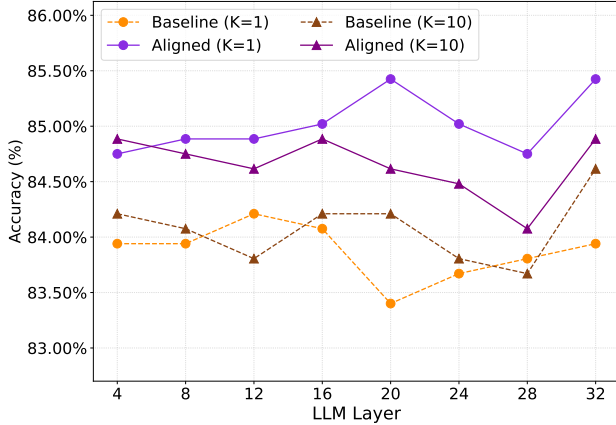


Figure 3. KNN classification accuracy of point cloud tokens extracted from different LLM layers on ModelNet40. We compare the baseline model and our aligned model using $K=1$ and $K=10$.

demonstrate that our model generates accurate descriptions with details about object geometry, materials, and attributes. In the QA examples, the model correctly answers questions that require both visual understanding and external knowledge. The bolded text indicates accurate predictions that capture specific characteristics of the 3D objects.

Table 3 presents a qualitative comparison of outputs from different models on a representative sample. In this sample, 2D models and early 3D methods exhibit significant recognition deviations. Our model not only accurately determines the cartoon style of the dinosaur but also provides detailed descriptions of anatomical features such as sharp teeth and claws, recognizes the open mouth posture, and infers its attacking or defensive state along with potential application domains. These improvements stem from the partial token alignment mechanism that enforces consistency between intermediate layer representations and Q-Former outputs during training. This enables the model to retain richer point cloud semantic features rather than discarding valuable information due to insufficient textual supervision.

4.5. Ablation Study

In this section, ablation studies are first conducted to validate the key design choices of the alignment regularization method. Additional analyses are then performed to examine the quality of learned representations and data efficiency.

Loss function. We compare three distance metrics at layer 16, including L1, L2, and cosine similarity. As shown in Table 4, cosine similarity achieves the best average accuracy of 66.08%, outperforming L1 by 0.36 pp and L2 by 0.51 pp. Cosine loss focuses on directional consistency rather than numerical differences, making it more suitable for LLM hidden representations where point cloud tokens undergo multiple transformations while maintaining semantic consistency with Q-Former outputs.

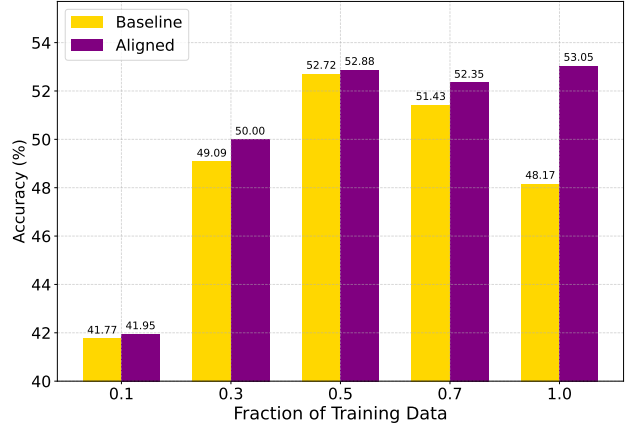


Figure 4. Impact of training data fraction on 3D object captioning performance. We evaluate baseline and aligned models using 10%, 30%, 50%, 70%, and 100% of training data on Objaverse dataset.

Target layer. We evaluate alignment at layers 8, 12, 16, 20, 24, 28, and 32. Additionally, we test joint alignment at multiple layers 12, 16, and 20 simultaneously. As shown in Table 5, layer 16 achieves the strongest performance with an average accuracy of 66.08%, showing 0.75 pp improvement over layer 8 and 0.94 pp improvement over layer 12. Deeper layers from 20 to 32 exhibit gradual performance degradation, with layer 28 dropping 1.27 pp compared to layer 16. This indicates that intermediate layers are most effective for processing 3D visual information. Joint alignment at layers 12, 16, and 20 decreases performance by 1.74 pp, suggesting that simultaneous constraints at multiple layers introduce conflicting optimization objectives.

Alignment weight. We investigate the impact of the alignment loss weight λ at layer 16 using cosine similarity. As shown in Table 6, $\lambda = 0$ (NTP loss only, without alignment) yields 64.72%, while $\lambda = 0.1$ achieves the best average accuracy of 66.08%, confirming that the gains stem from alignment regularization rather than merely Stage-2 training. Higher weights from 0.3 to 0.9 lead to consistent performance drops, with $\lambda = 0.7$ decreasing accuracy by 1.69 pp. This suggests that excessive alignment constraints overly restrict the model’s capacity to fuse point cloud features with linguistic representations, while a smaller weight preserves sufficient flexibility for cross-modal feature integration. This flexibility appears crucial, as performance on the instruction-based Objaverse task drops by 3.0 pp as soon as λ increases from 0.1 to 0.3.

Number of linear layers. We examine the impact of the projector architecture at layer 16 by varying the number of linear layers from 1 to 4. As shown in Table 7, 3 linear layers achieve optimal performance with an average accuracy of 66.08%, improving 1.63 pp over a single layer and 0.60 pp over two layers. The 4 layer configuration shows slight degradation to 65.24%, indicating that deeper projec-

Table 7. Ablation study on the number of linear layers in the alignment projector. We evaluate the impact at layer 16 on classification accuracy using cosine similarity loss with $\lambda = 0.1$.

Num. Layers	ModelNet40		Objaverse		Average
	(I)	(C)	(I)	(C)	
1	61.47	60.82	70.50	65.00	64.45
2	61.26	61.67	71.00	68.00	65.48
3	61.55	60.78	72.50	69.50	66.08
4	61.43	61.02	70.00	68.50	65.24

Table 8. Ablation study on the alignment target. We evaluate the impact of different alignment targets at layer 16 on classification accuracy (%) using cosine similarity loss with $\lambda = 0.1$.

Loss	ModelNet40		Objaverse		Average
	(I)	(C)	(I)	(C)	
q-former	61.55	60.78	72.50	69.50	66.08
Projector-mid	62.16	60.70	69.50	68.00	65.09
Projector	61.79	60.33	70.00	67.50	64.91

tors risk overfitting. This accuracy of 65.24% is notably lower than even the 2 layer model’s performance, which strongly suggests the added complexity is detrimental. The 3 layer architecture provides adequate modeling capacity to bridge the representation gap between Q-Former and LLM hidden states without introducing unnecessary complexity.

Alignment target. We compare three alignment targets at layer 16, including Q-Former outputs, intermediate projector features, and final projector outputs. As shown in Table 8, aligning with Q-Former outputs yields the best average accuracy of 66.08%, outperforming intermediate projector features by 0.99 pp and final projector outputs by 1.17 pp. Q-Former outputs preserve richer geometric semantics from point clouds, while intermediate and final projector features are increasingly adapted toward the LLM input space, losing discriminative 3D structural information critical for downstream classification tasks.

Feature quality analysis. To further validate that alignment regularization improves the discriminative quality of point cloud tokens in LLM hidden layers, we conduct KNN classification experiments on ModelNet40. We extract point cloud tokens from layers 4, 8, 12, 16, 20, 24, 28, and 32 of both the baseline and aligned models, and evaluate their classification accuracy using K=1 and K=10 nearest neighbors. As shown in Figure 3, the aligned model outperforms the baseline across all evaluated layers for both K=1 and K=10 scenarios. For K=1, the aligned model achieves peak accuracy of 85.43% at layer 20, compared to the baseline’s 83.40% at layer 20, demonstrating a 2.03 pp improvement. For K=10, the aligned model reaches 84.62% at layer 12, while the baseline at 83.81% at layer 12. Notably, the aligned model demonstrates sustained superior

accuracy across the entire network depth, confirming that alignment regularization preserves richer discriminative geometric features throughout the LLM’s forward pass, leading to better performance on the downstream tasks.

Data efficiency. To assess the effectiveness of our alignment regularization under varying data availability, we conduct experiments on the 3D object captioning task using different fractions of training data from the Objaverse dataset. As shown in Figure 4, the aligned model consistently outperforms the baseline across all data regimes. With only 10% of training data, our method achieves 41.95% compared to the baseline’s 41.77%, demonstrating effectiveness even in highly data-scarce scenarios. At 30% data fraction, the aligned model gains 0.91 pp over the baseline. Most notably, with full training data, the aligned model achieves 53.05% accuracy compared to the baseline’s 48.17%, representing a substantial 4.88 pp improvement.

Critically, the baseline model exhibits a significant performance degradation from 52.72% (50% data) to 48.17% (100% data), losing 4.55 pp when provided with more training data. This suggests that the standard next-token prediction objective struggles to effectively utilize larger, more diverse datasets, potentially leading to optimization instability or overfitting. In stark contrast, our aligned model maintains consistent improvement across all data scales, reaching its peak performance at 100% data. This strongly indicates that our alignment regularization acts as an effective regularizer, stabilizing the training process and enabling the model to fully leverage increased data availability, rather than simply overfitting to a larger dataset.

5. Conclusion

In this work, we address the critical challenge of data scarcity in 3D vision-language models by proposing PointAlign, a feature-level alignment regularization method. By introducing explicit supervision at intermediate layers through Q-Former output alignment, our method effectively prevents geometric information degradation with minimal computational overhead. Extensive experiments validate the effectiveness of our approach, achieving 2.08 pp improvement on average for classification tasks across ModelNet40 and Objaverse datasets, with notable gains of 7.50 pp on open-vocabulary classification and 4.88 pp on captioning evaluated by Qwen2-72B-Instruct. These results demonstrate that feature-level supervision enables more effective utilization of limited 3D data and enhances generalization across diverse 3D understanding tasks.

Limitations. The quality of alignment is constrained by the representational capacity of the visual feature aggregation module. Additionally, the alignment at a single fixed layer and the simple loss may not optimally supervise the entire feature transformation process. Future work includes exploring multi-layer alignment strategies, contrastive learning, and learnable distance metrics.

References

- [1] Yukang Chen, Jianhui Liu, Xiangyu Zhang, Xiaojuan Qi, and Jiaya Jia. Voxelnext: Fully sparse voxelnet for 3d object detection and tracking. In *Proceedings of the IEEE/CVF Conference on Computer Vision and Pattern Recognition*, pages 21674–21683, 2023. 1
- [2] Zhenyu Chen, Ali Gholami, Matthias Nießner, and Angel X Chang. Scan2cap: Context-aware dense captioning in rgb-d scans. In *Proceedings of the IEEE/CVF conference on computer vision and pattern recognition*, pages 3193–3203, 2021. 12
- [3] Wenliang Dai, Junnan Li, Dongxu Li, Anthony Tiong, Junqi Zhao, Weisheng Wang, Boyang Li, Pascale N Fung, and Steven Hoi. Instructblip: Towards general-purpose vision-language models with instruction tuning. In *Advances in Neural Information Processing Systems*, pages 49250–49267, 2023. 1, 4, 5
- [4] Matt Deitke, Dustin Schwenk, Jordi Salvador, Luca Weihs, Oscar Michel, Eli VanderBilt, Ludwig Schmidt, Kiana Ehsani, Aniruddha Kembhavi, and Ali Farhadi. Objaverse: A universe of annotated 3d objects. In *Proceedings of the IEEE/CVF Conference on Computer Vision and Pattern Recognition*, pages 13142–13153, 2023. 5
- [5] Jiajun Deng, Tianyu He, Li Jiang, Tianyu Wang, Feras Dayoub, and Ian Reid. 3d-llava: Towards generalist 3d llms with omni superpoint transformer. In *Proceedings of the Computer Vision and Pattern Recognition Conference*, pages 3772–3782, 2025. 12
- [6] Runpei Dong, Zekun Qi, Linfeng Zhang, Junbo Zhang, Jianjian Sun, Zheng Ge, Li Yi, and Kaisheng Ma. Autoencoders as cross-modal teachers: Can pretrained 2d image transformers help 3d representation learning? *arXiv preprint arXiv:2212.08320*, 2022. 2
- [7] Stefan Elfving, Eiji Uchibe, and Kenji Doya. Sigmoid-weighted linear units for neural network function approximation in reinforcement learning. *Neural networks*, 107:3–11, 2018. 3, 4
- [8] Lue Fan, Feng Wang, Naiyan Wang, and Zhao-Xiang Zhang. Fully sparse 3d object detection. In *Advances in Neural Information Processing Systems*, pages 351–363, 2022. 1
- [9] Ziyu Guo, Renrui Zhang, Longtian Qiu, Xianzhi Li, and Pheng-Ann Heng. Joint-mae: 2d-3d joint masked autoencoders for 3d point cloud pre-training. *arXiv preprint arXiv:2302.14007*, 2023. 2
- [10] Ziyu Guo, Renrui Zhang, Xiangyang Zhu, Yiwen Tang, Xianzheng Ma, Jiaming Han, Kexin Chen, Peng Gao, Xianzhi Li, Hongsheng Li, et al. Point-bind & point-llm: Aligning point cloud with multi-modality for 3d understanding, generation, and instruction following. *arXiv preprint arXiv:2309.00615*, 2023. 2, 4, 5
- [11] Kaiming He, Xinlei Chen, Saining Xie, Yanghao Li, Piotr Dollár, and Ross Girshick. Masked autoencoders are scalable vision learners. In *Proceedings of the IEEE/CVF Conference on Computer Vision and Pattern Recognition*, pages 16000–16009, 2022. 2
- [12] Edward J Hu, Yelong Shen, Phillip Wallis, Zeyuan Allen-Zhu, Yuanzhi Li, Shean Wang, Lu Wang, and Weizhu Chen. LoRA: Low-rank adaptation of large language models. In *International Conference on Learning Representations*, 2022. 2
- [13] Tianyu Huang, Bowen Dong, Yunhan Yang, Xiaoshui Huang, Rynson WH Lau, Wanli Ouyang, and Wangmeng Zuo. Clip2point: Transfer clip to point cloud classification with image-depth pre-training. In *Proceedings of the IEEE/CVF International Conference on Computer Vision*, pages 22157–22167, 2023. 2
- [14] Wencan Huang, Daizong Liu, and Wei Hu. Fast3d: Accelerating 3d multi-modal large language models for efficient 3d scene understanding. *arXiv preprint arXiv:2507.09334*, 2025. 2
- [15] Xiaohu Huang, Jingjing Wu, Qunyi Xie, and Kai Han. Mllms need 3d-aware representation supervision for scene understanding. *arXiv preprint arXiv:2506.01946*, 2025. 2
- [16] Aaron Hurst, Adam Lerer, Adam P Goucher, Adam Perelman, Aditya Ramesh, Aidan Clark, AJ Ostrow, Akila Welihinda, Alan Hayes, Alec Radford, et al. Gpt-4o system card. *arXiv preprint arXiv:2410.21276*, 2024. 4, 5
- [17] Mojan Javaheripi, Sébastien Bubeck, Marah Abdin, Jyoti Aneja, Sebastien Bubeck, Caio César Teodoro Mendes, Weizhu Chen, Allie Del Giorno, Ronen Eldan, Sivakanth Gopi, et al. Phi-2: The surprising power of small language models. Microsoft Research Blog, 2023. 4
- [18] Zhangqi Jiang, Junkai Chen, Beier Zhu, Tingjin Luo, Yankun Shen, and Xu Yang. Devils in middle layers of large vision-language models: Interpreting, detecting and mitigating object hallucinations via attention lens. In *Proceedings of the IEEE/CVF Conference on Computer Vision and Pattern Recognition*, pages 25004–25014, 2025. 2
- [19] Omri Kaduri, Shai Bagon, and Tali Dekel. What’s in the image? a deep-dive into the vision of vision language models. In *Proceedings of the IEEE/CVF Conference on Computer Vision and Pattern Recognition*, pages 14549–14558, 2025. 1
- [20] Seil Kang, Jinyeong Kim, Junhyeok Kim, and Seong Jae Hwang. Your large vision-language model only needs a few attention heads for visual grounding. In *Proceedings of the IEEE/CVF Conference on Computer Vision and Pattern Recognition*, pages 9339–9350, 2025. 2
- [21] Fuhao Li, Wenxuan Song, Han Zhao, Jingbo Wang, Pengxiang Ding, Donglin Wang, Long Zeng, and Haoang Li. Spatial forcing: Implicit spatial representation alignment for vision-language-action model. *arXiv preprint arXiv:2510.12276*, 2025. 1, 2
- [22] Junnan Li, Dongxu Li, Silvio Savarese, and Steven Hoi. Blip-2: Bootstrapping language-image pre-training with frozen image encoders and large language models. In *International Conference on Machine Learning*, pages 19730–19742. PMLR, 2023. 1, 2, 3
- [23] Yingwei Li, Adams Wei Yu, Tianjian Meng, Ben Caine, Jiquan Ngiam, Daiyi Peng, Junyang Shen, Yifeng Lu, Denny Zhou, Quoc V Le, et al. Deepfusion: Lidar-camera deep fusion for multi-modal 3d object detection. In *Proceedings of the IEEE/CVF Conference on Computer Vision and Pattern Recognition*, pages 17182–17191, 2022. 1

- [24] Haotian Liu, Chunyuan Li, Qingyang Wu, and Yong Jae Lee. Visual instruction tuning. In *Advances in Neural Information Processing Systems*, pages 34892–34916, 2023. 4, 5
- [25] Minghua Liu, Ruoxi Shi, Kaiming Kuang, Yinhao Zhu, Xuanlin Li, Shizhong Han, Hong Cai, Fatih Porikli, and Hao Su. Openshape: Scaling up 3d shape representation towards open-world understanding. In *Advances in Neural Information Processing Systems*, pages 44860–44879, 2023. 2
- [26] Jiageng Mao, Shaoshuai Shi, Xiaogang Wang, and Hongsheng Li. 3d object detection for autonomous driving: A comprehensive survey. *International Journal of Computer Vision*, 131(8):1909–1963, 2023. 1
- [27] Zekun Qi, Runpei Dong, Guofan Fan, Zheng Ge, Xiangyu Zhang, Kaisheng Ma, and Li Yi. Contrast with reconstruct: Contrastive 3d representation learning guided by generative pretraining. In *International Conference on Machine Learning*, pages 28223–28243. PMLR, 2023. 2
- [28] Zekun Qi, Runpei Dong, Shaochen Zhang, Haoran Geng, Chunrui Han, Zheng Ge, Li Yi, and Kaisheng Ma. Shapellm: Universal 3d object understanding for embodied interaction. In *European Conference on Computer Vision*, pages 214–238. Springer, 2024. 1, 2, 5
- [29] Zhangyang Qi, Ye Fang, Zeyi Sun, Xiaoyang Wu, Tong Wu, Jiaqi Wang, Dahua Lin, and Hengshuang Zhao. Gpt4point: A unified framework for point-language understanding and generation. In *Proceedings of the IEEE/CVF Conference on Computer Vision and Pattern Recognition*, pages 26417–26427, 2024. 2, 4, 5
- [30] Christoph Schuhmann, Romain Beaumont, Richard Vencu, Cade Gordon, Ross Wightman, Mehdi Cherti, Theo Coombes, Aarush Katta, Clayton Mullis, Mitchell Wortsman, et al. Laion-5b: An open large-scale dataset for training next generation image-text models. In *Advances in Neural Information Processing Systems*, pages 25278–25294, 2022. 1
- [31] Hyun Oh Song, Yu Xiang, Stefanie Jegelka, and Silvio Savarese. Deep metric learning via lifted structured feature embedding. In *Proceedings of the IEEE/CVF Conference on Computer Vision and Pattern Recognition*, pages 4004–4012, 2016. 4
- [32] Yuanhao Su, Daoye Zhu, Zhande Dong, Qifeng Lin, Lingbo Liu, and Shuming Bao. Fame: Fusion of alignment and multi-view enhancement for remote sensing image-text retrieval. *IEEE Transactions on Geoscience and Remote Sensing*, 2025. 1
- [33] Yuan Tang, Xu Han, Xianzhi Li, Qiao Yu, Yixue Hao, Long Hu, and Min Chen. Minigpt-3d: Efficiently aligning 3d point clouds with large language models using 2d priors. In *Proceedings of the 32nd ACM International Conference on Multimedia*, pages 6617–6626, 2024. 1, 2, 3, 4, 5
- [34] Yuan Tang, Xu Han, Xianzhi Li, Qiao Yu, Jinfeng Xu, Yixue Hao, Long Hu, and Min Chen. More text, less point: Towards 3d data-efficient point-language understanding. In *Proceedings of the AAAI Conference on Artificial Intelligence*, pages 7284–7292, 2025. 1, 5
- [35] Qwen Team et al. Qwen2 technical report. *arXiv preprint arXiv:2407.10671*, 2(3), 2024. 5
- [36] Peter Tong, Ellis Brown, Penghao Wu, Sanghyun Woo, Adithya Jairam Vedagiri IYER, Sai Charitha Akula, Shusheng Yang, Jihan Yang, Manoj Middepogu, Ziteng Wang, et al. Cambrian-1: A fully open, vision-centric exploration of multimodal llms. In *Advances in Neural Information Processing Systems*, pages 87310–87356, 2024. 2
- [37] Fuying Wang, Yuyin Zhou, Shujun Wang, Varut Vardhanabhuti, and Lequan Yu. Multi-granularity cross-modal alignment for generalized medical visual representation learning. In *Advances in Neural Information Processing Systems*, pages 33536–33549, 2022. 1
- [38] Haochen Wang, Anlin Zheng, Yucheng Zhao, Tiancai Wang, Zheng Ge, Xiangyu Zhang, and Zhaoxiang Zhang. Reconstructive visual instruction tuning. *arXiv preprint arXiv:2410.09575*, 2024. 2
- [39] XuDong Wang, Xingyi Zhou, Alireza Fathi, Trevor Darrell, and Cordelia Schmid. Visual lexicon: Rich image features in language space. In *Proceedings of the IEEE/CVF Conference on Computer Vision and Pattern Recognition*, pages 19736–19747, 2025. 2
- [40] Ziyi Wang, Xumin Yu, Yongming Rao, Jie Zhou, and Jiwen Lu. Take-a-photo: 3d-to-2d generative pre-training of point cloud models. In *Proceedings of the IEEE/CVF International Conference on Computer Vision*, pages 5640–5650, 2023. 2
- [41] Zhirong Wu, Shuran Song, Aditya Khosla, Fisher Yu, Linguang Zhang, Xiaoou Tang, and Jianxiong Xiao. 3d shapenets: A deep representation for volumetric shapes. In *Proceedings of the IEEE/CVF Conference on Computer Vision and Pattern Recognition*, pages 1912–1920, 2015. 1, 5
- [42] Runsen Xu, Xiaolong Wang, Tai Wang, Yilun Chen, Jiangmiao Pang, and Dahua Lin. Pointllm: Empowering large language models to understand point clouds. In *European Conference on Computer Vision*, pages 131–147. Springer, 2024. 1, 2, 3, 4, 5
- [43] Le Xue, Mingfei Gao, Chen Xing, Roberto Martín-Martín, Jiajun Wu, Caiming Xiong, Ran Xu, Juan Carlos Niebles, and Silvio Savarese. Ulip: Learning a unified representation of language, images, and point clouds for 3d understanding. In *Proceedings of the IEEE/CVF Conference on Computer Vision and Pattern Recognition*, pages 1179–1189, 2023. 2
- [44] Le Xue, Ning Yu, Shu Zhang, Artemis Panagopoulou, Junnan Li, Roberto Martín-Martín, Jiajun Wu, Caiming Xiong, Ran Xu, Juan Carlos Niebles, et al. Ulip-2: Towards scalable multimodal pre-training for 3d understanding. In *Proceedings of the IEEE/CVF Conference on Computer Vision and Pattern Recognition*, pages 27091–27101, 2024. 2
- [45] Heeji Yoon, Jaewoo Jung, Junwan Kim, Hyungyu Choi, Heeseong Shin, Sangbeom Lim, Honggyu An, Chaehyun Kim, Jisang Han, Donghyun Kim, et al. Visual representation alignment for multimodal large language models. *arXiv preprint arXiv:2509.07979*, 2025. 1
- [46] Xumin Yu, Lulu Tang, Yongming Rao, Tiejun Huang, Jie Zhou, and Jiwen Lu. Point-bert: Pre-training 3d point cloud transformers with masked point modeling. In *Proceedings of the IEEE/CVF Conference on Computer Vision and Pattern Recognition*, pages 19313–19322, 2022. 4

- [47] Junyi Zhang, Charles Herrmann, Junhwa Hur, Luisa Polania Cabrera, Varun Jampani, Deqing Sun, and Ming-Hsuan Yang. A tale of two features: Stable diffusion complements dino for zero-shot semantic correspondence. In *Advances in Neural Information Processing Systems*, pages 45533–45547, 2023. [2](#)
- [48] Qinglun Zhang, Zhen Liu, Haoqiang Fan, Guanghui Liu, Bing Zeng, and Shuaicheng Liu. Flowpolicy: Enabling fast and robust 3d flow-based policy via consistency flow matching for robot manipulation. In *Proceedings of the AAAI Conference on Artificial Intelligence*, pages 14754–14762, 2025. [1](#)
- [49] Renrui Zhang, Ziyu Guo, Wei Zhang, Kunchang Li, Xupeng Miao, Bin Cui, Yu Qiao, Peng Gao, and Hongsheng Li. Pointclip: Point cloud understanding by clip. In *Proceedings of the IEEE/CVF Conference on Computer Vision and Pattern Recognition*, pages 8552–8562, 2022. [2](#)
- [50] Shaofeng Zhang, Feng Zhu, Junchi Yan, Rui Zhao, and Xiaokang Yang. Zero-cl: Instance and feature decorrelation for negative-free symmetric contrastive learning. In *International Conference on Learning Representations*, 2021. [2](#)
- [51] Shaofeng Zhang, Lyn Qiu, Feng Zhu, Junchi Yan, Hengrui Zhang, Rui Zhao, Hongyang Li, and Xiaokang Yang. Align representations with base: A new approach to self-supervised learning. In *Proceedings of the IEEE/CVF Conference on Computer Vision and Pattern Recognition*, pages 16600–16609, 2022.
- [52] Shaofeng Zhang, Qiang Zhou, Sitong Wu, Haoru Tan, Zhibin Wang, Jinfa Huang, and Junchi Yan. Cr2pq: Continuous relative rotary positional query for dense visual representation learning. In *International Conference on Learning Representations*, 2025. [2](#)
- [53] Xiangdong Zhang, Shaofeng Zhang, and Junchi Yan. Pcpmae: Learning to predict centers for point masked autoencoders. In *Advances in Neural Information Processing Systems*, pages 80303–80327, 2024. [2](#)
- [54] Xiangdong Zhang, Shaofeng Zhang, and Junchi Yan. Towards more diverse and challenging pre-training for point cloud learning: Self-supervised cross reconstruction with decoupled views. In *Proceedings of the IEEE/CVF International Conference on Computer Vision*, pages 28696–28706, 2025. [2](#)
- [55] Yuhang Zheng, Xiangyu Chen, Yupeng Zheng, Songen Gu, Runyi Yang, Bu Jin, Pengfei Li, Chengliang Zhong, Zengmao Wang, Lina Liu, et al. Gaussiangrasper: 3d language gaussian splatting for open-vocabulary robotic grasping. *IEEE Robotics and Automation Letters*, 2024. [1](#)
- [56] Xiangyang Zhu, Renrui Zhang, Bowei He, Ziyu Guo, Ziyao Zeng, Zipeng Qin, Shanghang Zhang, and Peng Gao. Pointclip v2: Prompting clip and gpt for powerful 3d open-world learning. In *Proceedings of the IEEE/CVF International Conference on Computer Vision*, pages 2639–2650, 2023. [2](#)

A. Additional Experiments

A.1. Generalization to Non-Q-Former Architectures

To validate that our alignment regularization is architecture-agnostic and not limited to Q-Former-based models, we apply our method to 3D-LLaVA [5], which uses Omni Superpoint Transformer (OST) with MLP instead of Q-Former, on the Scan2Cap [2] dataset for scene-level 3D dense captioning. As shown in Table 9, our method yields consistent improvements across all four metrics, with CIDEr@0.5 improving by 2.7, demonstrating effectiveness beyond object-level tasks and Q-Former architectures.

Table 9. Scene-level 3D dense captioning on Scan2Cap [2]. Our alignment regularization is applied to 3D-LLaVA [5], which does not use Q-Former. (* denotes reproduced results.)

Method	C@0.5	B-4@0.5	M@0.5	R@0.5
3D-LLaVA*	76.1	36.3	27.0	57.3
+ Ours	78.8	37.1	27.2	57.6

A.2. Generalization to Different LLM Backbones

To verify that the middle-layer alignment strategy generalizes across LLM architectures, we conduct layer selection experiments on Phi-3 (32 layers). As shown in Table 10, middle layers (12–20) generally outperform both early and late layers. This aligns with our Phi-2 ablation (Table 5) where Layer 16 achieves optimal results, demonstrating that the strategy is robust across different LLM backbones.

Table 10. Layer selection ablation on Phi-3 backbone. Middle layers generally achieve better performance, aligning with the Phi-2 results in Table 5.

Layer	ModelNet40		Objaverse		Average
	(I)	(C)	(I)	(C)	
MiniGPT-3D	62.50	56.50	57.13	48.03	56.04
8	65.00	56.50	57.18	49.59	57.07
12	66.00	56.00	58.74	49.35	57.52
16	65.50	56.00	58.69	48.66	57.21
20	66.00	56.00	58.51	49.27	57.45
24	65.00	55.00	57.82	49.31	56.78
28	63.50	54.00	58.10	48.95	56.14